

Exploring the Focusing Mechanism of the NuMI Horn Magnets

Katsuya Yonehara,* Sudeshna Ganguly, and Don Athula Wickremasinghe
Fermi National Accelerator Laboratory, Batavia, IL 60510, USA

Pavel Snopok and Yiding Yu
Illinois Institute of Technology, Chicago, IL 60616, USA
(Dated: May 16, 2023)

Neutrinos at the Main Injector (NuMI) is a project at Fermilab that provides an intense beam of neutrinos used by a number of experiments. NuMI creates a beam of pions that decay into neutrinos, muons, and other particles. Muons are registered by the muon monitors. Magnetic horns are the key elements of the NuMI beam line. This paper uses the muon beam profile observed at the muon monitors to study the NuMI horn focusing mechanism. It is found that the horn magnet generates dipole and quadrupole fields to focus pions. This suggests that the optics of the horn magnet are predominantly linear. Our study shows that the muon beam profile accurately detects the horn current within $\pm 0.05\%$.

I. INTRODUCTION

Fermilab hosts the world's most powerful accelerator-produced neutrino beam facility to characterize neutrino properties. The Neutrinos at the Main Injector (NuMI) facility operates an intense proton beam striking the high-power target to produce positively and negatively charged pions via hadronic interactions. The primary pion decay process for neutrino production is as follows:

$$\begin{aligned}\pi^+ &\rightarrow \nu_\mu + \mu^+, \\ \pi^- &\rightarrow \bar{\nu}_\mu + \mu^-.\end{aligned}$$

A magnetic horn plays a crucial role in the neutrino beamline to select pions of the correct charge, collect them in a wide energy range of 1–20 GeV, and transport them to a decay volume to provide the correct desired flavor and chirality¹ neutrinos to the neutrino detectors. Given its pivotal role, the horn needs to produce a high-reliability and high-stability magnetic field with low systematic uncertainty. Currently, the NuMI neutrino beam is provided to the NOvA [1, 2], MicroBooNE [3, 4], and ICARUS [5, 6] detectors. The physics tolerance of the beam-related systematic uncertainty on the neutrino measurement at NOvA detectors has been estimated [7]. Table I shows the range of beam parameters that stay within the physics tolerance. The beam instrumentation to measure the beam parameters is also shown [8].

A set of conventional detectors is used as the primary beam instrumentation to monitor the beam parameters with accuracy shown in Table I. However, in the event of a signal fluctuation in the detector, there is no method to check the signal quality. Therefore, the presence of secondary beam detectors that measure the beam parameters using a different method are a great advantage in cross-checking measurements.

This paper shows that the NuMI horn magnet generates dipole and quadrupole fields to focus pions. This suggests that the horn magnet optics is predominantly linear. Therefore, the phase space evolution of pions and muons in the NuMI beamline can be simulated using a linear beam optics model. The three muon monitors downstream of a hadron absorber after the decay volume (see Fig. 1) will be used as the secondary beam instrumentation. Each monitor measures a profile of the muon beam produced as a result of pion decay anywhere in the NuMI beam line. As Figure 1 shows, the thickness of the absorber material in front and between the monitors is different. As a result, each muon monitor detects muons of a different energy spectrum. Consequently, the beam profile observed by the corresponding monitor can be attributed to the magnet focusing strength at different pion energies. The observed profile at each monitor responds to the variation of beam parameters independently. By analyzing the muon monitor signal, the horn current is detected to $\pm 0.05\%$ accuracy. The other beam parameters in Table I are also detected from the monitor signal with high accuracy. Cross-checking beam measurements using different types of instrumentation and methods can effectively reduce beam-related systematic uncertainties, making it a viable technique for future neutrino experiments, such as Fermilab's Long Baseline Neutrino Facility (LBNF) [9, 10].

The main components of the NuMI beamline are introduced in Sec. II. The NuMI horn focusing mechanism is investigated by using analytical and numerical methods in Sec. III. The observed beam response at the muon monitors is described in Sec. IV. The beam parameters are determined from the muon monitor signal by using machine learning, which is demonstrated in Sec. V. Finally, we conclude the study and discuss future prospects in Sec. VI.

* yonehara@fnal.gov

¹ We omit the discussion of right-handed neutrinos or left-handed anti-neutrinos in this paper.

TABLE I. Estimated physics tolerance for the beam parameters of the NOvA experiment and the corresponding beam instrumentation. Here CT is a current transformer, BPM is a beam position monitor, and PM is a beam profile monitor. POT stands for the protons on target.

Beam parameter	Design value	Tolerance	Beam instrument	Accuracy
Horn current	200 kA	± 2 kA	Horn CT	0.1%
Horiz. beam position on target	0 mm	± 1 mm	BPM	0.02 mm
Vertical beam position on target	0 mm	± 1 mm	BPM	0.02 mm
RMS beam spot size	1.3 mm	± 0.2 mm	Beam PM	0.1 mm
Beam intensity	50×10^{12} POT	1%	Beam CT	0.5% (stability 0.1%)

II. NUMI BEAM COMPONENTS

Figure 1 shows the layout of the NuMI target and horn system, including the muon monitors. Every 1.2 seconds, a 120-GeV/ c proton beam is transported from the Main Injector to the NuMI target system. The beam spill length is 9.6 μ s. The highest beam intensity is 5.6×10^{13} protons on target (POT) per spill demonstrated in Spring 2022. The proton beam structure in the Main Injector and the NuMI proton beam transport line optics are described in [8]. In the following subsections, we discuss the main beam components and their relation to the study of the horn focusing mechanism.

A. NuMI target and horn system

Figure 2 shows the layout of the baffle, target canister, and Horn 1 in the NuMI beamline. The baffle is a 1.5-meter-long graphite cylinder with a 15-mm-diameter center hole along the beam axis to capture any mis-steered beam. The target canister is a water-cooled aluminum cylinder filled with atmospheric-pressure Helium gas that contains the target core. A thin Beryllium foil is used at both ends of the canister to make upstream and downstream beam windows. The thickness of the downstream window in which the beam particles pass through is 0.25 mm.

Figure 3 shows the target core made of a series of graphite fins (grade: POCO ZXF-5Q, density: 1.78 g/cm³). The nominal beam position at the target core is near the upper end of the fin. The first two fins are used for the beam position measurement. They can be electrically isolated from the ground so that the beam position can be measured by observing the intensity of the delta-rays knocked out from the fins by the incident beam. The next four fins have a thick graphite cylinder around the top of the fin. The cylinder diameter, 18 mm, is slightly larger than the inner center hole diameter of the baffle. These fins are called winged fins. A mis-steered proton beam hits the winged fin to reduce the beam intensity produced by multiple scattering. This way, the beam makes less thermal impact on the beam elements downstream from the target, which are not designed to receive the full intensity of the proton beam. The rest of the target core has 44 rounded rectangular

target fins. The length and width of the fins are 25 and 9 mm, respectively. The dimensions of the fin are determined from a balance between the pion production yield and thermal stress on the fin. The edge of the fin is rounded to avoid a shock wave concentration at a corner. The present target core is capable of operating with a 1-MW proton beam. The target core length is 1.25 m, and it has 48+2 fins along the beam direction.

Figure 4 shows the elevation view of the target hall. There are two horns called Horn 1 and Horn 2, respectively. Each horn is 3 m long and consists of two coaxial aluminum conductors. Figure 5 is the cross-sectional view of Horn 1. The inner conductor has a parabolic shape at each end of the horn, and there is a narrow straight cylindrical tube (called the “neck”) to connect the two parabolic shape conductors at both parabolic vertices; the outer conductor is a straight cylinder. The upstream end of the horn has a curved conductor that connects the inner and outer conductors continuously. A stripline conductor is connected at the downstream end of the horn to inject and extract the current. Horns 1 and 2 are electrically connected in series.

A Forward Horn Current (FHC) mode or neutrino mode occurs when the horn current flows in the inner conductor in the same direction as the beam. In this mode, a toroidal magnetic field is induced between the inner and outer conductors in the clockwise direction, focusing positively charged pions (Fig. 5). Negatively charged pions are focused in the Reverse Horn Current (RHC) mode, also known as the antineutrino mode. In this case, the horn current flows in the inner conductor in the opposite direction of the beam. To check the quality of the magnetic field in the horn, the radial magnetic field is measured at the neck before the horn is exposed to the beam. The observed magnetic field strength agrees with the analytical field calculation to within 0.1% [11]. Because the high-energy pions tend to travel in the forward direction of the proton beam, they often traverse inner diameter of the neck where no magnetic field exists. Some of them are wrong-charge pions since they generate wrong chirality neutrino events in the neutrino detectors. In addition to that, a small fraction of electron neutrinos produced in the decays of kaons and muons are also contained in the neutrino flux. The overall contamination of the neutrino beam is a few percent.

The inner conductor is cooled by a water jet sprayed

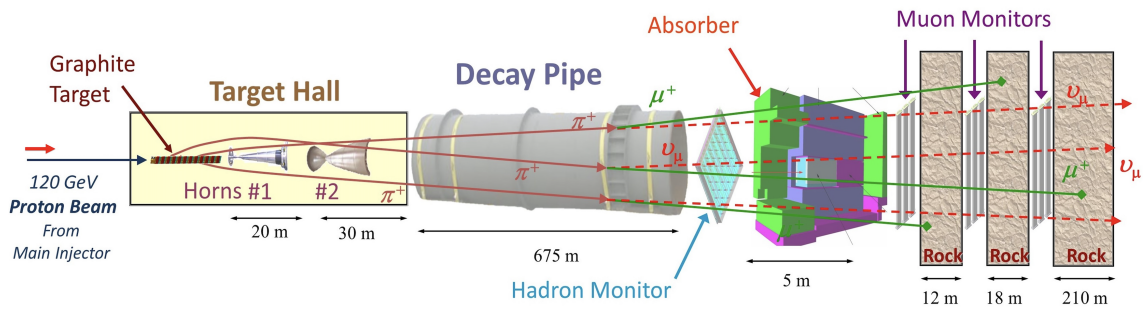


FIG. 1. The overall layout of the NuMI beamline.

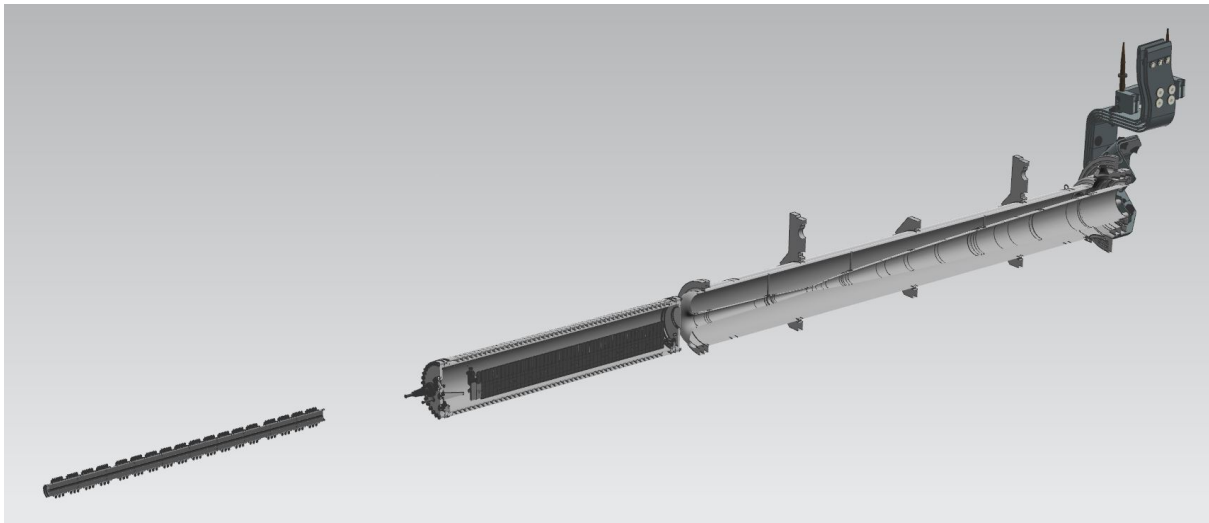


FIG. 2. The layout of the baffle, target chase, and Horn 1.

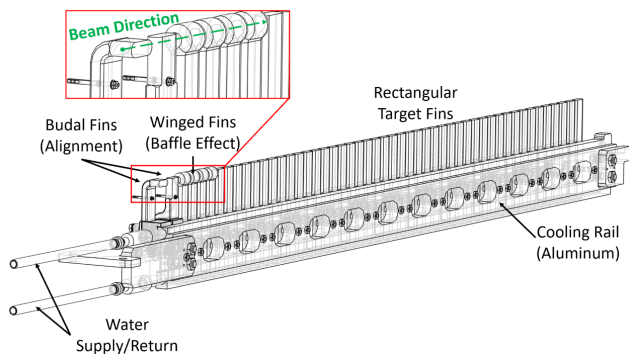


FIG. 3. The layout of the target core.

vertically from the outer conductor. Atmospheric-pressure Argon gas is contained between the inner and outer conductors. Argon gas is used because it has a higher electrical breakdown voltage than Helium gas.

The radial size of Horn 2 is larger than that of Horn 1. Detailed dimensions are shown in Sec. III B. The distance between the two horns is 20 m. The upstream end of the decay pipe is located 25 m downstream of Horn 2. The decay pipe contains an atmospheric-pressure Helium gas,

and most pions decay in the pipe. The length and inner diameter of the pipe are 675 m and 2 m, respectively, and there are 1.6-mm-thick Al windows on both ends of the pipe for sealing.

The first beam monitor, known as the hadron monitor, is located at the downstream end of the decay pipe. Presently, the hadron monitor is mainly used for the proton beam-based alignment [8, 12]. The positions of the target and horns are identified via proton beam tomography. The accuracy of the beam-based alignment is typically ± 0.1 mm. It is consistent with the optical survey result performed whenever a beam element is installed or replaced in the beamline.

Figure 6 shows the schematic drawing of the absorber, which is located right after the hadron monitor. It is essentially a box approximately $5.5 \text{ m} \times 5.6 \text{ m} \times 8.5 \text{ m}$ ($W \times H \times L$). The core volume is composed at its upstream end of eight $1.3 \text{ m} \times 1.3 \text{ m} \times 0.3 \text{ m}$ ($W \times H \times L$) aluminum blocks followed by ten $1.3 \text{ m} \times 1.3 \text{ m} \times 0.23 \text{ m}$ ($W \times H \times L$) flame-cut steel blocks. Each aluminum block has two independent water circuits, while the steel layers are not water-cooled. The function of the steel blocks is to catch the tails of the hadronic showers created in the core. Radiation shielding is provided by 88 steel blocks sur-

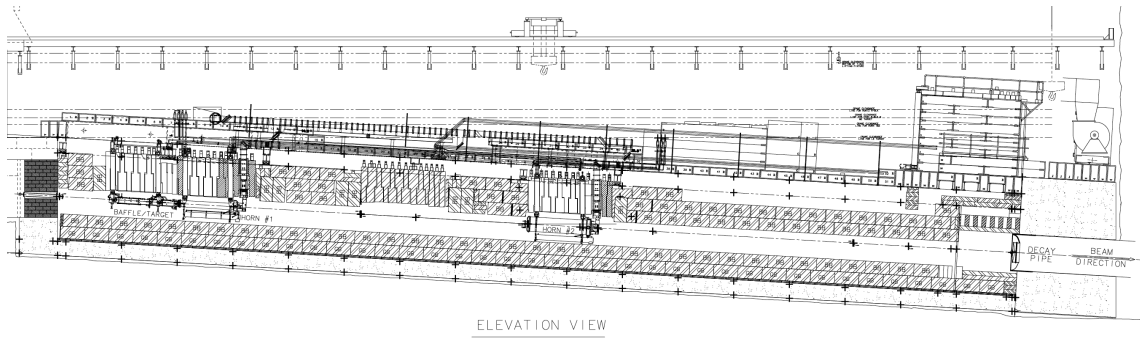


FIG. 4. The elevation view of the target hall. The beam axis is tilted by 58 mrad downward to direct the beam toward the Soudan Mine in Minnesota, where the MINOS far detector was located.

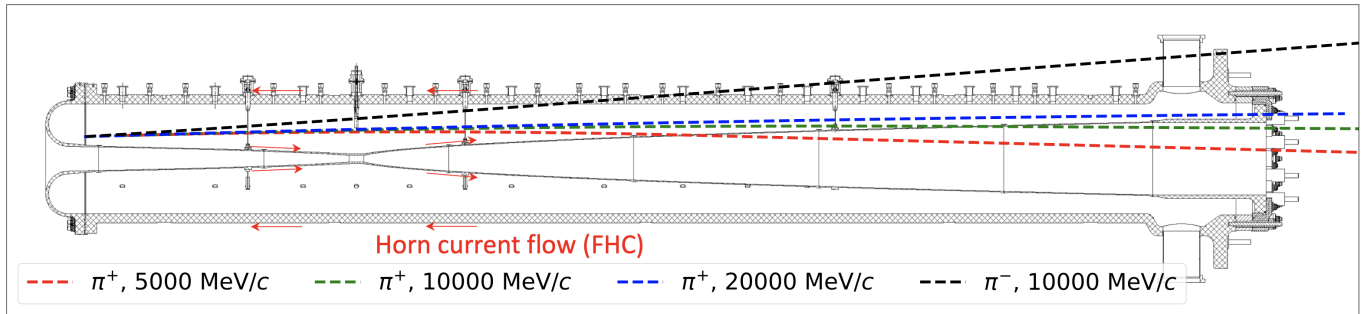


FIG. 5. The cross-sectional view of Horn 1. A red arrow near the horn conductor shows a horn current flow for the FHC mode. Trajectories of pions with different initial momenta. Red: 5 GeV/c, green: 10 GeV/c, blue: 20 GeV/c, black: wrong-sign pion of 10 GeV/c is defocused by the horn running in the FHC mode.

rounding the absorber core and absorbing thermal and low-energy neutrons, which iron is relatively transparent to. This double-layer absorber structure is shown in the simulated muon flux in the muon monitor (Fig. 7).

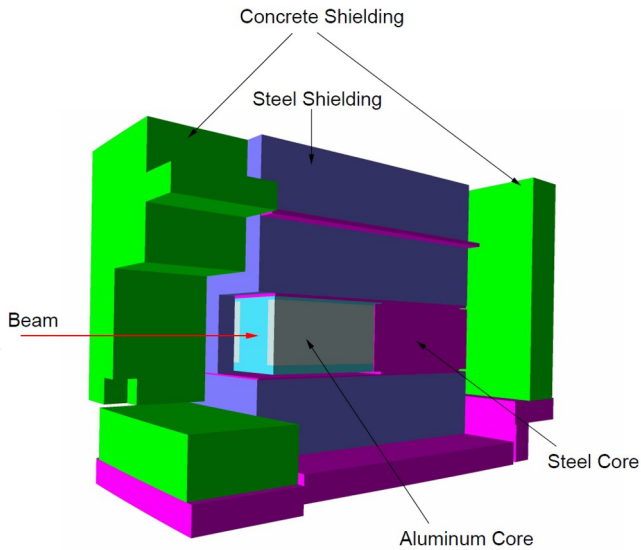


FIG. 6. The layout of the NuMI beam absorber.

There are three beam monitors after the absorber.

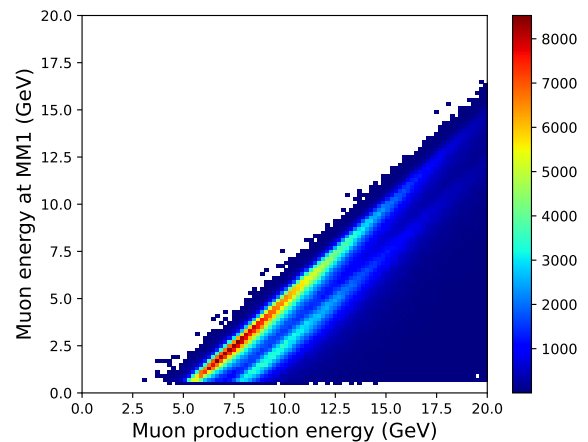


FIG. 7. Simulated 2D histogram of the muon spectrum. The horizontal axis is the muon energy at production, and the vertical axis is the muon energy at Muon Monitor 1. The thick band is the muons passing through the Aluminum core, while the second thin band is the muons passing through the steel block outside the Al core. Muons lose more energy in steel than Al.

Most charged particles produced upstream of the absorber are removed in the absorber volume except for

muons. Because these monitors mostly detect muons, they are called muon monitors. The first (the most upstream) muon monitor is called Muon Monitor 1 (MM1), the second Muon Monitor 2 (MM2), and the last Muon Monitor 3 (MM3). A detailed description of the muon monitors is given in Sec. IIB3. All residual charged particles, including muons, are stopped in the rock downstream of the muon monitors. Only neutrinos pass through the rock.

B. NuMI Beam Instrumentation

The primary beam instrumentation and the muon monitors for this study are described in this section.

1. Proton beam monitor

A pair of induced-charge pickup electrodes and a multi-wire Secondary Emission electron Monitor (SEM) are used as a beam position monitor (BPM) and beam profile monitor (PM), respectively. A special PM, which is permanently placed upstream of the target, is made of a thin ($5\mu\text{meter}$ thick \times $25\mu\text{meter}$ wide) Ti foil to mitigate the beam scattering at the foil. There are 47×47 foils stretched in x and y directions with gaps between foils of 0.5mm . The PM provides the proton beam profile for every spill. Other PMs are periodically inserted in the beam line at different locations for monitoring the beam optics.

Horizontal and vertical BPMs are paired to measure the beam position on the transverse plane. Two sets of paired BPMs near the target are used for measuring the proton beam position and beam orientation at the target. Several BPMs comprise a network system to automatically correct the proton beam position and beam orientation at the target, which is called the autotune [8]. The accuracy of the beam position measurement is $\pm 0.02\text{mm}$ using BPM and PM [8], and the accuracy of the RMS beam spot size measurement is $\pm 0.1\text{mm}$ using PM.

2. Current monitor

The proton beam intensity at the target is measured by using a toroidal beam Current Transformer (beam CT) located upstream of the target. The signal calibration is done by using a current source and by comparison to a Direct-Current Current Transformer (DCCT) at the Main Injector. The accuracy of the beam CT is 0.5% while the stability of signal pulse-per-pulse is $\pm 0.1\%$ [8, 13].

The horn power supply circuit generates a half-sinusoidal voltage, and the pulse is propagated through four striplines. The total pulse length of this half sinusoidal wave is 2.334msec . A current transformer measures the horn current for each stripline (horn CT). The

current transformer is calibrated using a pre-calibrated current source. The accuracy of horn CT is $\pm 0.1\%$ [14].

3. Muon monitors

Figure 8 shows a schematic drawing of the muon monitor. Each muon monitor consists of a 9×9 grid of ionization chambers. Each chamber has a $7.5 \times 7.5\text{cm}^2$ sense

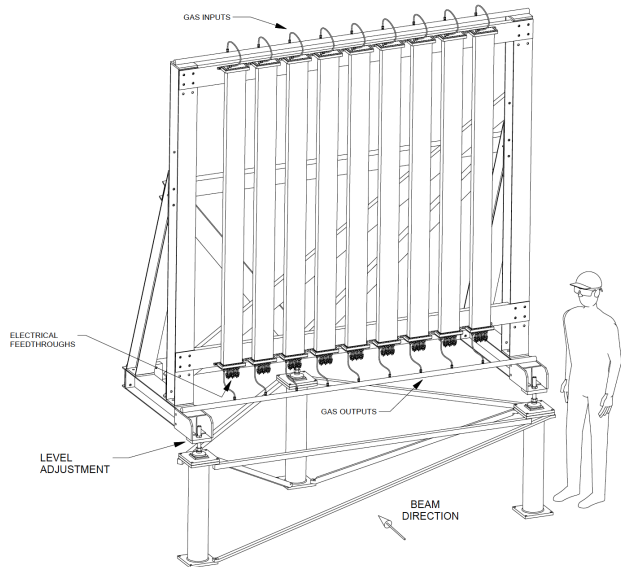


FIG. 8. Muon monitor engineering drawing showing the nine tubes containing a row of nine pixels each.

area Ag-Pt plated electrode on a 1-mm-thick Alumina ceramic electrode base, and the gap between the electrodes is 3mm . The distance between the centers of channels is 250mm to cover a $2.1 \times 2.1\text{m}^2$ area. Nine ionization chambers are installed in a rectangular aluminum tube. There are nine tubes assembled vertically on a support structure in the beam line. Atmospheric-pressure 99.995% pure Helium gas is used as an ionization media, injected from the top and exhausted from the bottom of each tube. The bias voltage is 300V in which the ionization chamber is on the plateau where all ionized charged particles in the chamber are collected at the electrodes without charge multiplication [15, 16].

Figures 9–11 show an example of the observed pixel image per spill. The pedestal signal, taken when the beam is turned off, is subtracted from the beam-on signal. The size of the pedestal signal is on the order of 0.1% as compared to the beam signal. The signal for each channel was calibrated using a radiation source before the monitor was installed in the beam line. The integrated signal from all channels is normalized by the beam intensity per beam spill and is monitored during beam operation. The long-term fluctuation of the integrated signal normalized by the beam intensity is $\pm 0.2\%$ for Muon Monitors 1 and 2 while the fluctuation of normalized Muon Monitor

3 signal is slightly higher at $\pm 0.5\%$. It is found that the observed pixel image pattern is not changed by the beam intensity although the signal size is proportional to the beam intensity.

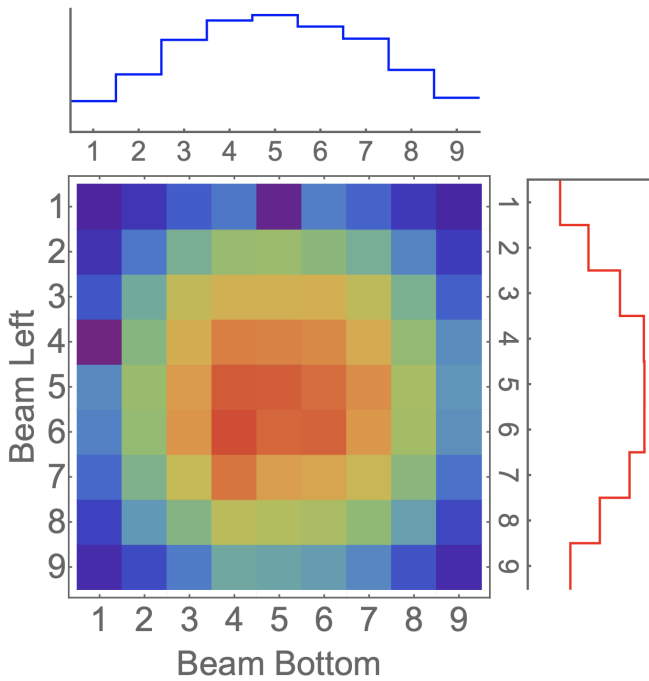


FIG. 9. The observed beam profile at Muon Monitor 1. The top and right subplots show the projection of the beam profile in horizontal and vertical planes, respectively.

The muon monitors are located downstream of the hadron absorber and separated by 12 and 18 m of rock (see Fig. 1). The muons reaching the monitors lose part of their kinetic energy in the material via energy loss processes. Therefore, the initial spectrum of muons when they are produced differs from the spectrum at the monitors. Figure 12 suggests that each monitor detects a different muon phase space with a specific cutoff energy. It is demonstrated in Sec. III that the observed beam profile on the monitors is the result of different horn magnet focusing strengths for different pion energies. Figures 13–15 show the simulated phase space of the initial pions for which the daughter muons reach the corresponding muon monitor. Muon Monitor 1 detects the initial pion momentum range above $5 \text{ GeV}/c$, Muon Monitor 2 detects the pion momentum range above $12 \text{ GeV}/c$, and Muon Monitor 3 detects the pion momentum above $25 \text{ GeV}/c$. It should be noted that the observed muon profile on the monitor is a result of the multiple Coulomb scattering in matter. As a result, muon signals are not correlated with specific neutrino events.

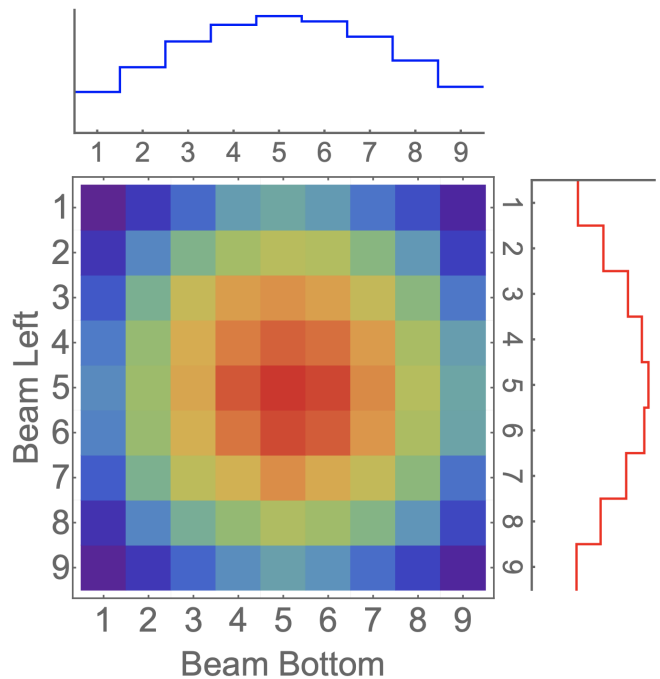


FIG. 10. The observed beam profile at Muon Monitor 2. The top and right subplots show the projection of the beam profile in horizontal and vertical planes, respectively.

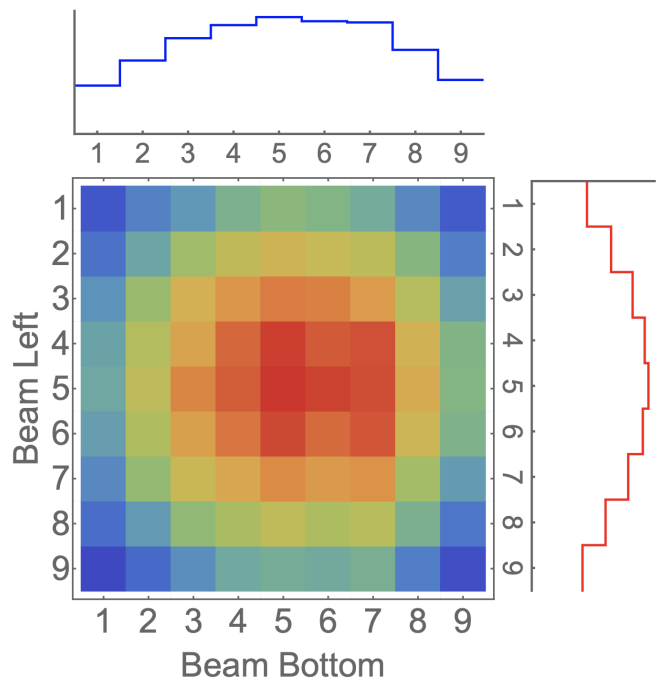


FIG. 11. The observed beam profile at Muon Monitor 3. The top and right subplots show the projection of the beam profile in horizontal and vertical planes, respectively.

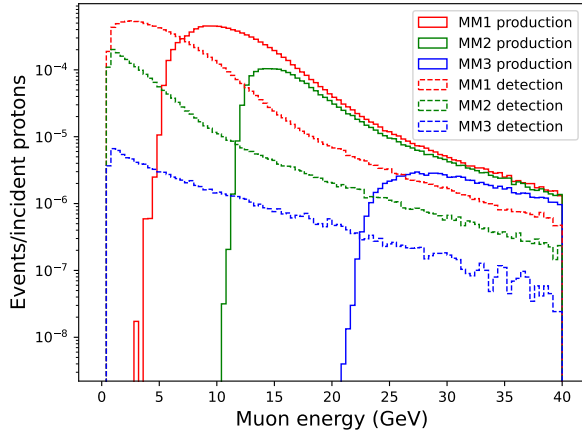


FIG. 12. Simulated muon spectra. A solid red line represents the muon spectrum when muons are produced while a dashed red line is the muon spectrum at Muon Monitor 1. The shift is because muons are lost energy in the absorber. The green and blue lines are for Muon Monitor 2 and 3, respectively.

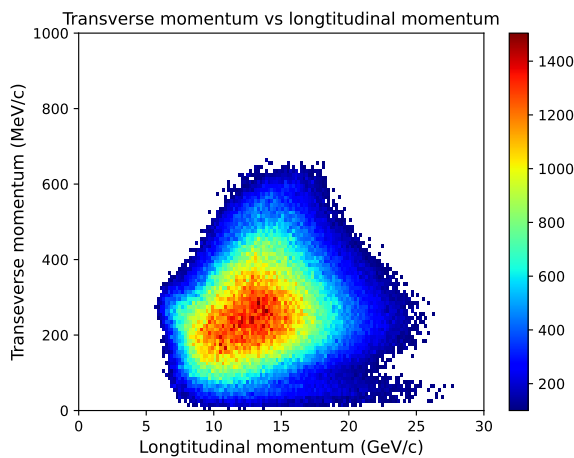


FIG. 13. Simulated transverse and longitudinal momenta of the pions for which the corresponding muons reach Muon Monitor 1. It should be noted that the low statistic bin is cut and set to be zero in the plot.

III. HORN FOCUSING MECHANISM

To maximize the sensitivity of neutrino oscillation and CP violation measurements, modern focusing horn systems are designed using numerical simulations. However, analyzing the horn focusing mechanism is challenging due to the complexity of the optimized system. For example, the target is not a point source, and the pion phase space received in the horn is broad. Additionally, the optimized horn itself has a complicated shape. These issues make it difficult to accurately model the particle trajectories. To better understand the mechanism, we start by using an

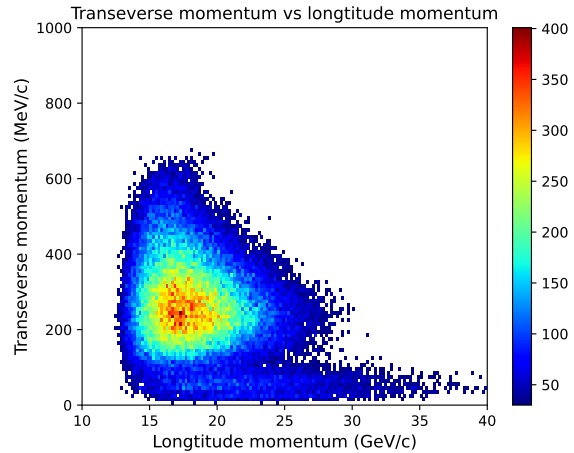


FIG. 14. Simulated transverse and longitudinal momenta of the pions for which the corresponding muons reach Muon Monitor 2.

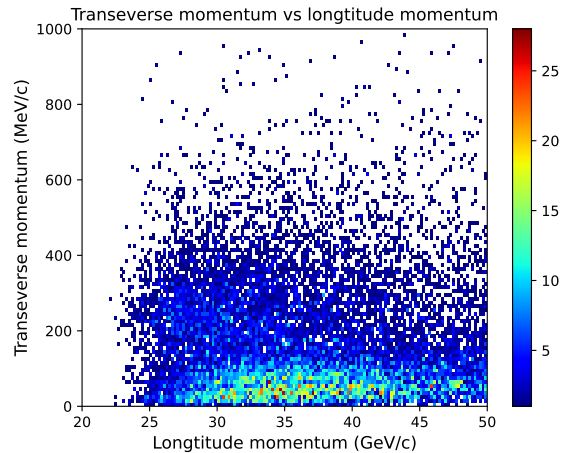


FIG. 15. Simulated transverse and longitudinal momenta of the pions for which the corresponding muons reach Muon Monitor 3.

analytical model formulated with a conventional beam optics method. A second-order polynomial function is employed to describe the mechanism in this model.

Next, we execute a simple simulation in which pions are ray-traced through the two horns using an analytical formula. This is therefore a semi-analytical model. By applying various assumptions in both models, the horn focusing strength is generalized and we can evaluate the acceptance of horn system without executing numerical simulations. However, we lose the accuracy of beam dynamics. The analytical and semi-analytical models are evaluated with a numerical ray-trace simulation in G4beamline [17], in which pions are tracked in a realistic horn field and horn conductor material. The mean energy loss is taken into account in the pion tracking in matter. However, the simulations do not include

stochastic processes such as decay, hadronic interaction, or multiple scattering.

Finally, the full model simulation is executed by using the modified G4NuMI framework to simulate all stochastic processes, including decay, hadronic interactions, and Coulomb interactions in the whole NuMI beamline. The acceptance of the NuMI horn system is evaluated by comparing the numerical simulation to the semi-analytical model. It is found that those results are in good agreement.

A. Analytical model

A horn conductor generates a toroidal magnetic field between the inner and outer conductors. As a result, an axially symmetric Lorentz force acts on charged particles. We use a cylindrical coordinate system (r, z, ϕ) . A particle trajectory in a long coaxial transmission line has been studied [18] in which the particle follows a spiral orbit in the space available between inner and outer conductors. In this paper, the angular momentum is ignored ($\phi' \sim 0$) in the model because the NuMI horn is too short to make a periodic motion around the horn inner conductor. A similar treatment is illustrated in Section 5.2.2 in the textbook *Particle Accelerator Physics* by Helmut Wiedemann.[19]

We start from the equation of motion in the transverse direction,

$$\frac{dp_r}{dt} = \frac{dp_r}{dz} \frac{dz}{dt} = \frac{dp_r}{dz} v_z = -qv_z b_\phi, \quad (1)$$

where p_r is the transverse momentum, v_z is the longitudinal velocity, and b_ϕ is the toroidal magnetic field.

The equation is simplified by using $\frac{dp_r}{dz} = -qb_\phi$, or $dp_r = -qb_\phi dz$. By inserting $dp_r \equiv p_r - p_{r,0}$ or $p_r = p_{r,0} + dp_r$ and $p_r = \gamma m \frac{dr}{dt} = \gamma m \frac{dz}{dt} \frac{dr}{dz} = p_z \frac{dr}{dz}$, where p_z is the longitudinal momentum, the equation is transformed:

$$p_z \frac{dr}{dz} = p_{r,0} - qb_\phi dz, \quad (2)$$

$$\frac{dr}{dz} = \frac{p_{r,0}}{p_z} - \frac{qb_\phi dz}{p_z}. \quad (3)$$

Here $p_{r,0}$ is the initial transverse momentum (and we assume $p_{z,0} \sim p_z$). By replacing $\frac{dr}{dz} \rightarrow \theta$ and $\frac{p_{r,0}}{p_z} \rightarrow \theta_0$, the equation becomes

$$\theta = \theta_0 - \frac{qb_\phi dz}{p_z}. \quad (4)$$

Eq. (4) shows the evolution of the angle of a charged particle in a horn field. The horn toroidal field is

$$b_\phi = \frac{\mu_0 I}{2\pi r}. \quad (5)$$

Thus, in Eq. (4) with a constant horn current, θ is a function of p_z , r , and dz :

$$\theta(p_z, r, dz) = \theta_0 - \frac{q\mu_0 I}{2\pi} \frac{dz}{p_z r}. \quad (6)$$

dz is the projection of pass length of a charged particle along z axis. In the following section, it is found that the NuMI magnetic horn works as a beam focusing element. The length of the horn is relatively short by comparing with the distance from the horn to the monitors. Therefore, a thin lens approximation is applied in the analytical model in which dz loses the information about z position, but is represented as a function of r . In the textbook, $dz \sim ar^2$ is used for presenting the desired focusing properties of the magnetic horn with a constant magnetic field strength, where a is a quadratic coefficient. To generalize the focusing properties, we assume that dz is a polynomial function of r :

$$dz \equiv a_0 + a_1 r + a_2 r^2 + a_3 r^3 + O(r^4), \quad (7)$$

where a_0, a_1, a_2 and a_3 are constants. a_0 is set to be zero in the model to avoid a singularity at $r = 0$. Hence,

$$\frac{dz}{r} = a_1 + a_2 r + a_3 r^2, \quad (8)$$

where the first, second, and third terms represent the expansion's dipole, quadrupole, and sextupole components, respectively. The particle angle after the transverse kick θ is

$$\theta(p_z, r, \theta_0) = \theta_0 - \frac{q\mu_0 I}{2\pi p_z} (a_1 + a_2 r + a_3 r^2). \quad (9)$$

Eq. (9) suggests that the horn acts as a multipole magnet. The distance of the charged particle from the horn to the crossing of the beam axis is

$$\lambda(p_z, r, \theta_0) = \frac{r}{\tan \theta} \sim \frac{r}{\theta} = \frac{r}{\theta_0 - \frac{q\mu_0 I}{2\pi p_z} (a_1 + a_2 r + a_3 r^2)} \quad (10)$$

Thus, the particle direction is parallel to the beam axis when $\lambda \rightarrow \pm\infty$ (or $\theta \rightarrow \pm 0$). Figure 16 shows the schematic drawing of the geometry used in the analytical model.

B. Semi-analytical model

The NuMI beamline has two horns, and each horn's shape is parabolic at both ends of the horn (Fig. 5). However, the analytical model only represents a single horn. A semi-analytical model is proposed to take into account the geometrical complications. The transverse kick in the magnetic horn is modeled by using the formula

$$\theta_k = q \frac{\int b_\phi dl}{p_z}, \quad (11)$$

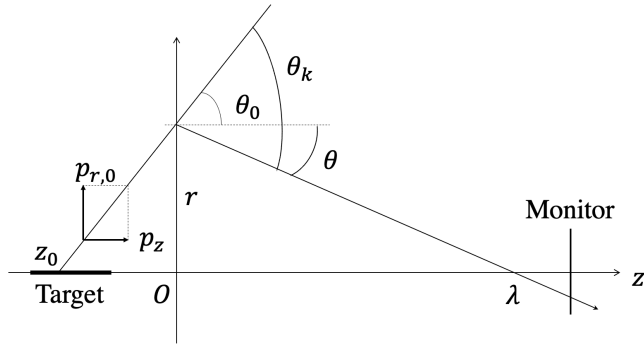


FIG. 16. Schematic drawing of the geometry which is used in the analytical model. “O” in the drawing is the horn position in the model.

where dl is the path length of a particle in the magnetic volume of the horn. Again, we use the assumption that the trajectory of a particle in the magnetic volume of the horn is parallel to the horn axis. Hence, the integrated magnetic field along the path length $\int b_\phi dl$ is analytically estimated by calculating the intersection points of a particle with the horn conductors while the magnetic field strength b_ϕ is a constant. The dimensions of the NuMI horns are summarized in Table II. The outer radii of Horn 1 and Horn 2 are 174.6 and 395.4 mm, respectively.

C. Test linear optics model

The particle tracking simulation uses G4beamline [17] to test the linearity of the NuMI horn optics and compare it with the analytical and semi-analytical models. In the simulation, a horn has a conductor material, and a magnetic field (given in Eq.(5)) is applied between inner and outer conductors where atmospheric-pressure Ar gas is contained. Test particles (pion) are distributed in

TABLE II. Magnetic horn profile for Horn 1 and Horn 2.

	z (mm)	profile (mm)
Horn 1	$0.00 \leq z < 80.00$	$\sqrt{\frac{92.85 - z}{7.05}}$
	$80.00 \leq z < 83.98$ (neck)	1.35
	$83.98 \leq z < 300.00$	$\sqrt{\frac{z - 80.00}{2.19}}$
Horn 2	$0.00 \leq z < 97.62$	$\sqrt{\frac{100.00 - z}{0.14}} - 0.30$
	$97.62 \leq z < 104.80$ (neck)	3.90
	$104.80 \leq z < 300.00$	$\sqrt{\frac{z - 100.00}{0.27}} - 0.30$

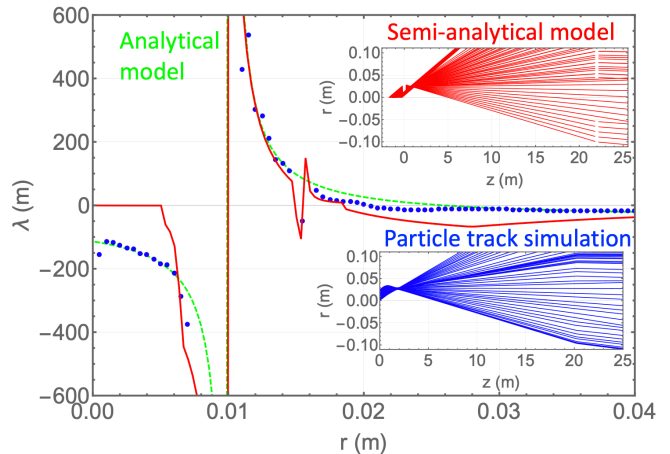


FIG. 17. Simulated λ as a function of the initial radial position r for a pion with $p_z = 12$ GeV/c and $p_{r,0} = 0.2$ GeV/c. Blue points: particle track simulation, solid red line: semi-analytical model, dashed green line: analytical model. Top subplot: ray trace of pions with the semi-analytical model, bottom plot: ray trace of pions using the particle tracking simulation.

front of Horn 1 (“O” in Fig. 16 is the upstream end of Horn 1 in the particle track simulation). The initial test particle position is distributed with a 0.5 mm step in the radial direction (a vertical axis in Fig. 16). The initial transverse and longitudinal momenta are variable parameters to fill the possible initial pion phase space escaped from the target.

Figure 17 shows the estimated λ as a function of the initial radial particle position r in the particle track simulation (a blue point), semi-analytical model (a solid red curve), and analytical model (a dashed green curve) for a pion with $p_z = 12$ GeV/c and $p_{r,0} = 0.2$ GeV/c. The semi-analytical model reproduces the particle tracking simulation result at $r > 0.01$ m. Besides, the semi-analytical model reproduces the second singularity point around $r = 0.015$ m. This is caused by the transverse kick in Horn 2 after crossing the beam axis. It is shown in the ray-trace in both subplots in Fig. 17, where pions are kicked by Horn 2 around $z = 20$ m and $r = -0.05 \sim -0.10$ m in the semi-analytical model and the particle track simulation. On the other hand, the semi-analytical model is not well reproduced λ at $r < 0.01$ m because all test particles below $r < 0.01$ m in the semi-analytical model miss the horns due to the thin lens model, which is not the case in the particle track simulation.

The coefficients of the analytical model are found from the fitting of the particle track simulation result. These are $a_1 = 0.0061$, $a_2 = 0.069$, and $a_3 = 0.0$. As the fitting is conducted at a singularity point, the fitting coefficient is determined by minimizing the chi-square value. In this case, the fitting error is considered to be significantly small and is therefore omitted. However, we found that the sextupole coefficient has a wide range of low

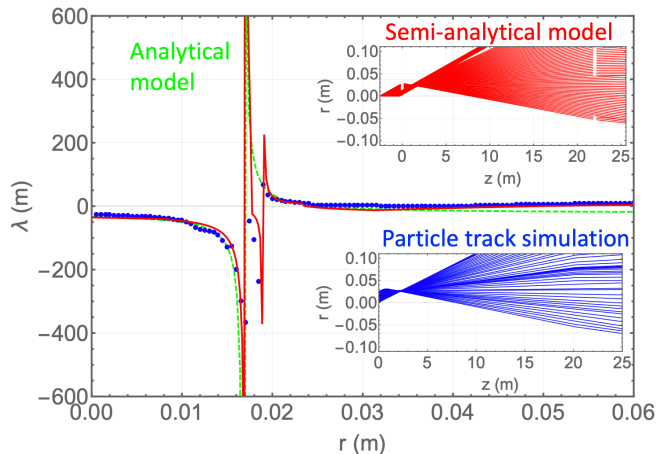


FIG. 18. Simulated λ as a function of the initial radial position r for a pion with $p_z = 18 \text{ GeV}/c$ and $p_{r,0} = 0.2 \text{ GeV}/c$. Blue points: particle track simulation, solid red line: semi-analytical model, dashed green line: analytical model.

chi-square values. This suggests that the sextupole coefficient is not sensitive to changes in the λ curve.

The semi-analytical model reproduces the complicated particle tracking in higher momentum regions while it does not work well at lower momenta. Figure 18 shows the estimated λ for a pion with $p_z = 18 \text{ GeV}/c$ and $p_{r,0} = 0.2 \text{ GeV}/c$. There are two singularity points in this case. The semi-analytical model precisely reproduces these points as well as the complicate λ curve at $r = 0.016 \sim 0.02 \text{ m}$. The best fitting of the analytical model is made at $a_1 = 0.0063$, $a_2 = 0.12$, and $a_3 = 2.7 \times 10^{-4}$. It should be noted that pions at $r < 0.01 \text{ m}$ miss Horn 1 while they are focused by Horn 2 so λ has a negative value. The focusing mechanism is observed in both subplots.

On the other hand, Figure 19 shows the estimated λ for a pion with $p_z = 10 \text{ GeV}/c$ and $p_{r,0} = 0.3 \text{ GeV}/c$. The estimated λ in the semi-analytical model is underestimated by comparison with the particle track simulation. The transverse kick to a particle in the semi-analytical model is found to be stronger than in the particle track simulation. As a result, the estimated λ in the semi-analytical model tends to be shorter. It is also found that the estimated λ for low momentum particle is sensitive to the gaps between the target and Horn 1, and Horn 1 and Horn 2. The fitting coefficients of the analytical model are $a_1 = 0.0061$, $a_2 = 0.048$, and $a_3 = 1.5 \times 10^{-5}$.

The fitting of the analytical model suggests that the singularity behavior is reproduced well by the dipole and quadrupole components, while the sextupole component is negligibly small. Consequently, the linear optics model is a good approximation for the particle track in the NuMI horn system. It is found that the coefficient of the quadrupole component is changed by the momentum. It will represent a chromaticity of the horn. Further study

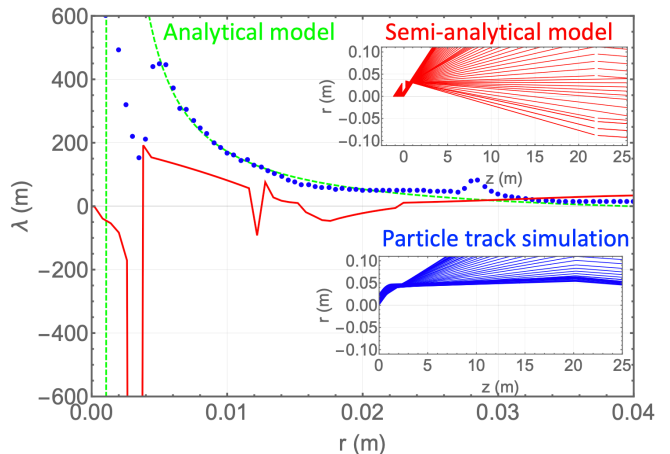


FIG. 19. Simulated λ as a function of the initial radial position r for a pion with $p_z = 10 \text{ GeV}/c$ and $p_{r,0} = 0.3 \text{ GeV}/c$. Blue points: particle track simulation, solid red line: semi-analytical model, dashed green line: analytical model.

is in progress.

D. Acceptance study of the NuMI horn system

The acceptance of the NuMI horn system is executed in the full model simulation. The modified G4NuMI is used. G4NuMI contains the most updated NuMI beam elements for the neutrino flux simulation. The modified G4NuMI can track muons and duplicate pion events multiple times to increase the statistics of muon events. The decay and kinematics of daughter particles in the duplicated pions are independently executed using the normal Geant4 processes.

The full model simulation starts with the primary protons impinging on the target. The acceptance is defined by the initial phase space of the pions right after escaping from the target, for which the decay products (muons) reach the muon monitors. On the other hand, the initial beam in the semi-analytical model is comprised of pions. The initial position of pions is uniformly distributed on the surface of the target volume along the z axis. The initial transverse and longitudinal momenta are uniformly distributed. Therefore, the semi-analytical model only evaluates the boundary of the acceptance. The energy cut is taken into account in the semi-analytical model for low momentum pions. Figure 20 shows the comparison of the full model simulation where the acceptance is shown as a 2D histogram with the semi-analytical model for which the boundary of the acceptance is outlined with a red dashed line. Both simulations are in good agreement.

There is a mismatch in the high p_z region. Most pions which have $p_z = 25 \text{ GeV}/c$ or higher can reach the absorber without decay. Most of those pions are absorbed in the absorber. A small fraction of pions are converted

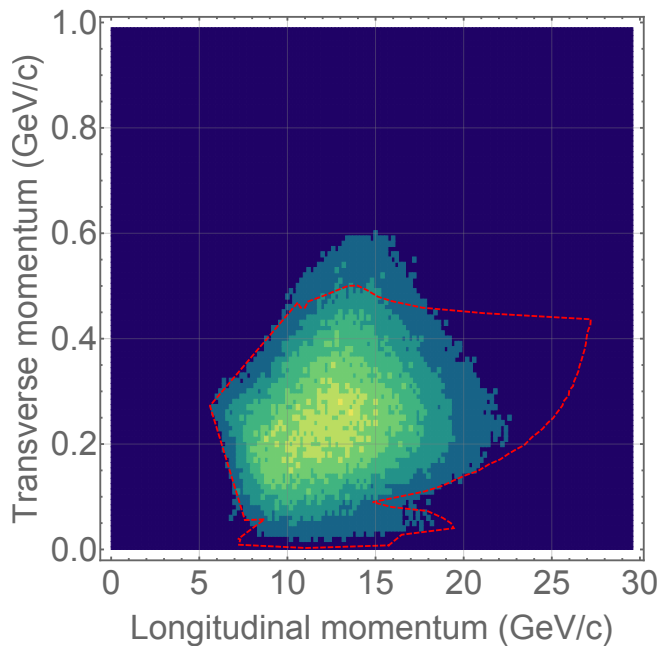


FIG. 20. Full model simulation result (2D histogram) vs. semi-analytical model (red dashed boundary outline).

into high energy muons. The semi-analytical model does not take into account the pion loss process in the absorber. Indeed, high momentum pions are shown in the spectrum of Muon Monitor 2 (Fig. 14) which is low statistics by comparing Muon Monitor 1. The acceptance of the semi-analytical model represents well the combined spectrum of Muon Monitor 1 and 2. The estimated λ shows that low p_z particles have a different tracking between the semi-analytical model and the numerical simulation in the previous subsection. Such a discrepancy is too small to affect the acceptance.

The semi-analytical model is used to further develop our acceptance studies. Figure 21 demonstrates how the acceptance of pions is influenced by their initial position upon emission from the target. The blue area shows the acceptance for which pions are emitted from the first 1/3 of the target length. The green area shows the acceptance for which pions are emitted from the middle 1/3 of the target length. The orange area shows the acceptance for which pions are emitted from the last 1/3 of the target length. Higher-momentum pions are more likely to be emitted from the first third of the target length, while lower-momentum pions are predominantly emitted from the last third of the target length. It suggests that the time domain muon profile measurement at the muon monitors shows the phase space of pions produced in a specific target section. The early (late) arriving muons at the monitor will be the result of the decay of high (low) energy pions which could be produced at the last (first) third of target. We are considering using a picosecond detector to measure the time domain muon profile.

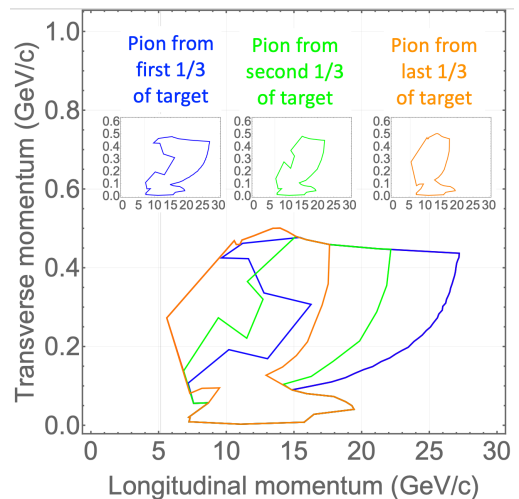


FIG. 21. Simulate the boundary of the acceptance of pions in the semi-analytical model. The acceptance of pions separated by the start position of pions within the target. Blue: pions start from the first 1/3 of the target length. Green: pions start from the middle 1/3 of the target length. Orange: pions start from the last 1/3 of the target length. Higher-momentum pions tend to start from the first 1/3 of the target length, while lower-momentum pions are extracted mostly from the last 1/3 of the target length.

IV. BEAM RESPONSE MEASUREMENT

The first systematic beam response measurement for studying the horn focusing mechanism was carried out on December 12, 2019, by changing the beam position at the target and the horn current. The procedure is as follows:

- Place the horn in the FHC mode.
- Set the beam intensity lower than 4×10^{13} POT per beam spill. Limiting the beam intensity protects the target from a mis-steered beam.
- Move the proton beam position at the target in the horizontal and vertical directions. The beam orientation is kept parallel to the horn axis. The observed target center from the proton tomography measurement was (horizontal, vertical) = (0.0, -0.8) mm. The movement range of the beam position is typically ± 0.8 mm from the target center.
- Observe the beam centroid variation on each muon monitor as a function of the proton beam position at the target.
- Once the beam scan data was taken, vary the horn current. The horn current was set to 200, 195, 190, and 180 kA.

Figure 22 is the observed horizontal beam centroid at the muon monitors as a function of the horizontal proton beam position on target at a horn current of 200 kA. In

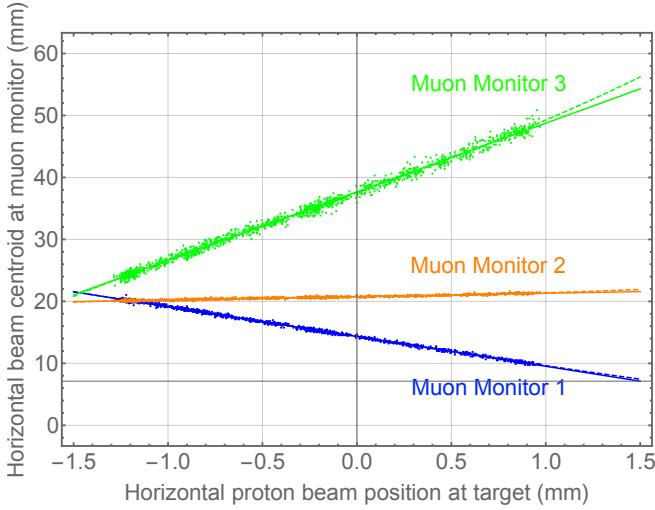


FIG. 22. The observed horizontal beam centroid at the muon monitor as a function of the horizontal proton beam position at the target. The horn current is 200 kA. Blue, orange, and green points are the observed beam centroids at Muon Monitors 1, 2, and 3, respectively. The solid line represents a linear fit, and the dashed line represents a third-order polynomial fit.

order to establish linearity, two types of fitting are used. The solid line is a linear fit and the dashed line is a fit with a third-order polynomial function. The fitting analysis shows that the horizontal beam centroid variation is linear. The variations of the intercepts at different monitors are caused by the imperfection of alignment for the beam element. They are not discussed in this study.

Muon Monitor 2 data are particularly interesting. The slope is almost zero. It suggests that the beam is in focus at Muon Monitor 2. A negative slope at Muon Monitor 1 shows that the beam is overfocused at Muon Monitor 1. In contrast, a positive slope at Muon Monitor 3 shows that the beam is underfocused at Muon Monitor 3, or the beam diverges. Thus, each muon monitor detects muons focused differently based on the parent pion energy. These phenomena are consistent with the linear optics model.

Figure 23 is the observed vertical beam centroid at the muon monitors as a function of the vertical proton beam position at the target at a horn current of 200 kA. The fitting analysis suggests that the observed beam centroid variation is still predominantly linear. However, a nonlinear component clearly appears, especially in the Muon Monitors 2 and 3. It should be noted that the target geometry is asymmetric in the vertical direction, so the variation of the vertical pion phase space should differ from the horizontal. This is evidenced by the results of the vertical beam scan. The nonlinear component is reproduced in the full model simulation. Overall, this is a good validation test of the physics processes in the full model simulation. A detailed study of validating the physics model will be presented in another paper.

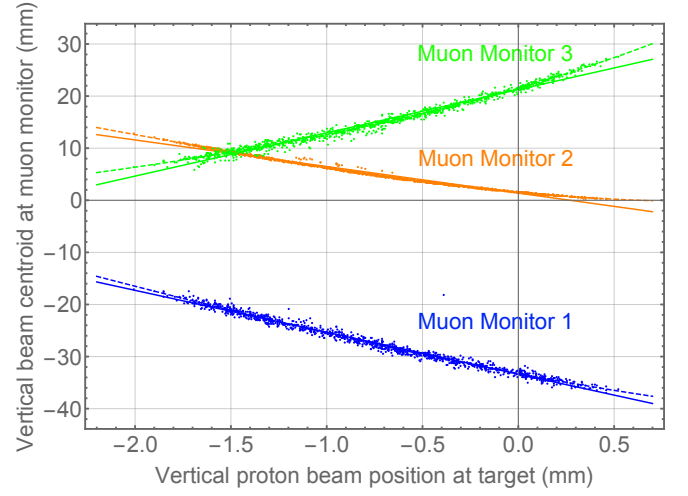


FIG. 23. The observed vertical beam centroid at the muon monitor as a function of the vertical proton beam position at the target. The horn current is 200 kA. Blue, orange, and green points are the observed beam centroids at Muon Monitors 1, 2, and 3, respectively. The solid line represents a linear fit, and the dashed line represents a third-order polynomial fit.

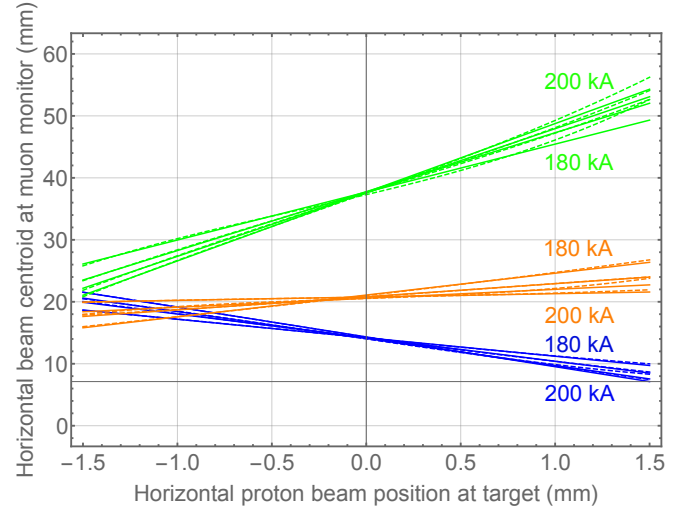


FIG. 24. The observed vertical beam centroid at the muon monitor as a function of the vertical proton beam position at the target at horn current 200, 195, 190, and 180 kA. Blue, orange, and green lines are the fits for beam centroids at Muon Monitors 1, 2, and 3, respectively. The solid line represents a linear fit, and the dashed line represents a third-order polynomial fit.

Figures 24 and 25 show the fitting curves of the observed horizontal and vertical beam centroid variations at different horn currents, respectively. Figures 26 and 27 show the measured slope for horizontal and vertical beam scans from the fitting analysis as a function of the horn current, respectively. A solid line is a result of linear fitting of the measured slope while a dashed line is the simulated slope by using the full model simulation. It is

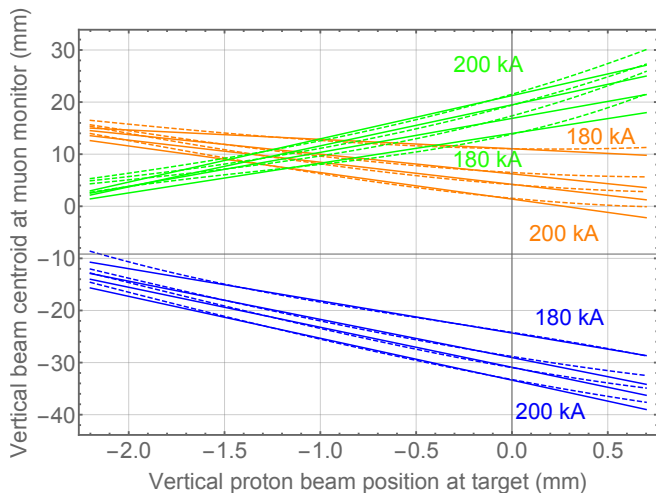


FIG. 25. The observed vertical beam centroid at the muon monitor as a function of the vertical proton beam position at the target at horn current 200, 195, 190, and 180 kA. Blue, orange, and green lines are the fits for beam centroids at Muon Monitors 1, 2, and 3, respectively. The solid line represents a linear fit, and the dashed line represents a third-order polynomial fit.

found that the slope is proportional to the horn current in the measurement and the simulation. The linear horn current dependence is predicted by the analytical model in Eq. 9.

Overall, the full model simulation reproduces the measured slope well. However, the simulation does not include two background processes [15]. A delta-ray which is generated in the material by interacting with high energy muons affects the muon monitor signal. Elastically scattered protons from the target produce additional particles in the absorber. Those background processes are included in a new simulation study. Fine tuning of the full model simulation does not affect the beam centroid result, but changes the muon beam profile. Further simulation study of these effects is in progress.

V. MACHINE LEARNING ALGORITHM TO DETECT BEAM PARAMETERS USING MUON MONITOR DATA

As demonstrated in the previous sections, the NuMI horn is a linear beam optics element. It suggests that the muon monitor response signal should be linearly related to the beam parameter variations. The muon monitor signal analysis is carried out by using a Machine Learning (ML) algorithm. An advantage of using ML for this application is that it finds correlations among a large number of input parameters and deconvolves them to make a prediction. For example, it is known that the beam intensity affects the horn current because the beam heats the horn conductor by the energy deposition and changes its conductance. By applying ML, the horn cur-

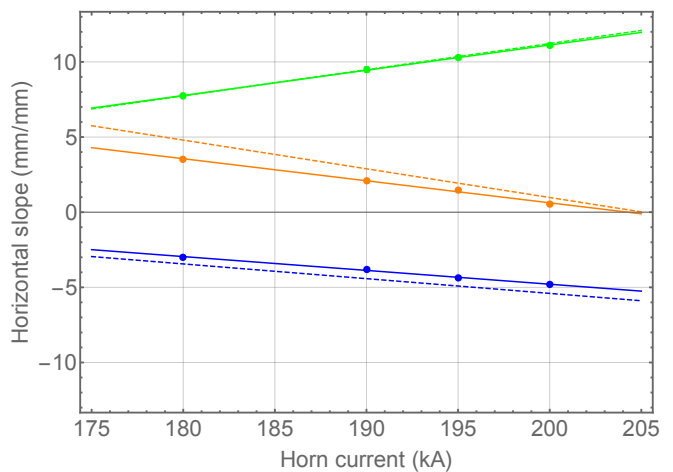


FIG. 26. The estimated slope from the horizontal beam scan as a function of the horn current. Blue, orange, and green points are the observed beam centroids at Muon Monitors 1, 2, and 3, respectively. Blue, orange, and green dashed lines are the simulated beam centroid at Muon Monitors 1, 2, and 3 in the full model simulation, respectively.

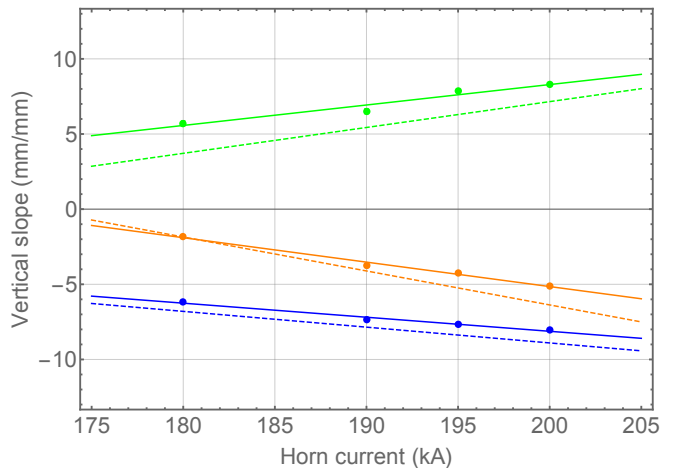


FIG. 27. The estimated slope from the vertical beam scan as a function of the horn current. Blue, orange, and green points are the observed beam centroid at Muon Monitors 1, 2, and 3, respectively. Blue, orange, and green dashed lines are the simulated beam centroid at Muon Monitors 1, 2, and 3 in the full model simulation, respectively.

rent and the beam intensity are detected independently from the observed muon profile.

An Artificial Neural Network (ANN) with multiple hidden layers is used to build the ML architecture. The ANN takes 241 observed values from individual muon monitor channels as inputs. It predicts four beam parameters: horn current, beam intensity, and horizontal and vertical beam positions at the target. Two dead channels on Muon Monitor 1, (row, column) = (1,5) and (4,1) in Fig. 9, are omitted in this analysis. The total number of data points prepared for the study is 13,563. The data is divided into training (70%) and validation (30%) data

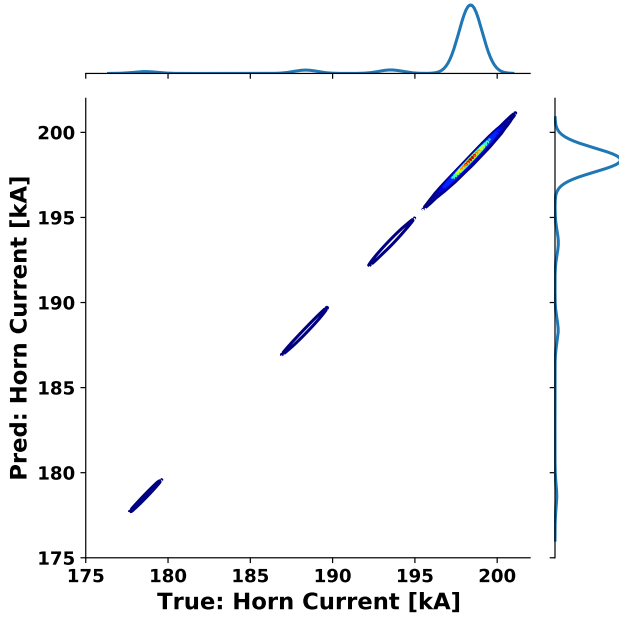


FIG. 28. Comparison of the predicted horn current from the muon monitor signal vs. the measured horn current by using the horn CT.

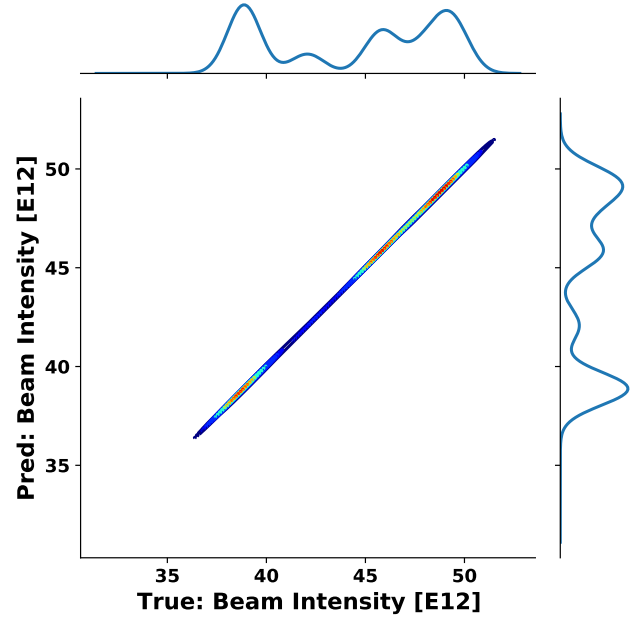


FIG. 29. Comparison of the predicted beam intensity from the muon monitor signal vs. the measured beam intensity using the beam CT. The units are 10^{12} protons per spill.

to optimize the ANN model architecture.

Figure 28 compares the measured horn current by using the horn current transformer (CT) and the predicted horn current by the trained ANN model. On the other hand, Figure 29 compares the beam current measured by the beam CT and the predicted beam intensity by the trained ANN model. These figures show that the horn current and the beam intensity are identified independently from the same validation data by applying the trained ANN model. It validates that ML can simultaneously detect the horn current and beam intensity from the observed muon profile.

Figures 30 and 31 show the measured and detected horn current and beam intensity as a function of time, respectively. The fluctuations observed in the signal of the primary beam instrumentation can be reproduced by the values detected using a trained ANN model. It suggests that the fluctuations are unlikely to be due to electrical noise but rather are likely to be associated with variations in the beam intensity and horn current stability. The accuracy of the estimated beam parameters from the ANN is $\pm 0.05\%$ for the horn current and $\pm 0.1\%$ for the beam intensity.

Figures 32 and 33 compare the horizontal and vertical beam positions at the target measured by using the BPM and detected by the trained ANN model, respectively. Again, the detection values reproduce the measurements well. It suggests that the signal fluctuation is the stability of the beam position at the target. The accuracy of ML detection is ± 0.018 mm and ± 0.013 mm for the horizontal and vertical positions, respectively.

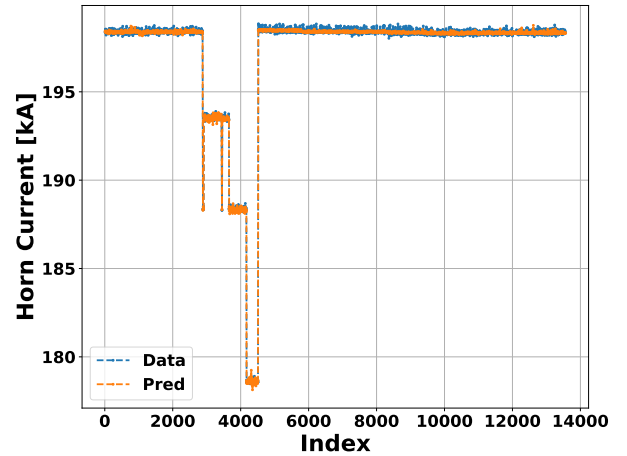


FIG. 30. Comparison between the observed horn current by using the horn CT and the predicted horn current from the muon monitor signal by using ML.

Table III shows that the muon monitor can detect all beam parameters affecting the NOvA experiment's physics tolerance. The accuracy of the Machine Learning (ML) detection from the muon monitor signal is similar to the accuracy of the primary beam instrumentation, which is shown in Table I. This implies that the ML method is able to provide reliable results that are comparable to the traditional methods of measuring the primary beam instrumentation.

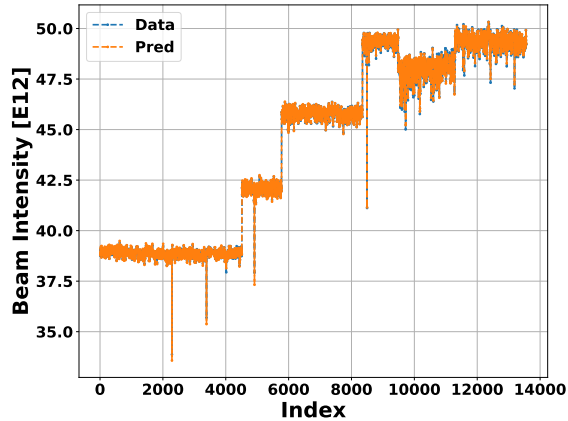


FIG. 31. comparison between the observed beam intensity by using the beam CT and the predicted beam intensity from the muon monitor signal by using ML.

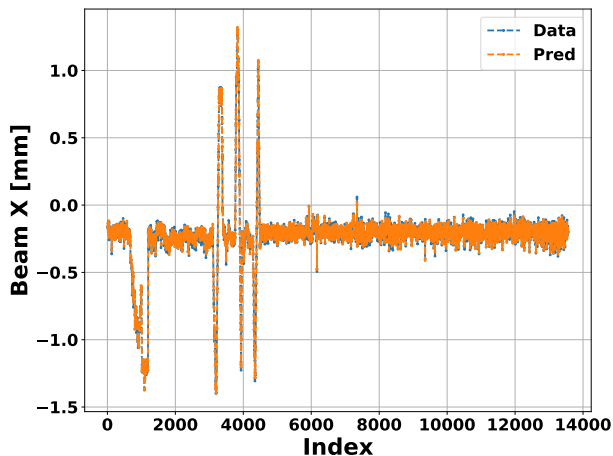


FIG. 32. Comparison between the horizontal beam position at the target observed by using the BPM and the horizontal proton beam positions predicted by using the ML.

From these studies, we confirm that ML has the potential to improve the ability to diagnose the NuMI target and horn system. One specific application of ML is to use it as an anomaly event detector, which can identify anomalies such as target density deterioration, target core damage, or degraded horn field quality. However, the accuracy of the ML detection is highly dependent on the quality of the training dataset. Therefore, it is important to optimize the ML architecture and reduce systematic errors in the training data to improve the accuracy of the model. These studies are underway.

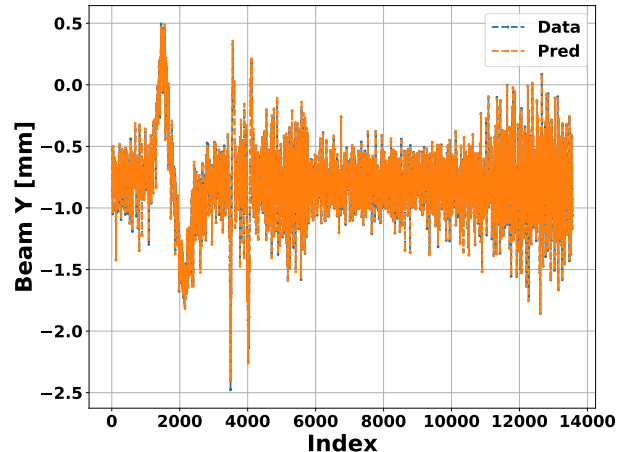


FIG. 33. Comparison between the vertical beam position at the target observed by using the BPM and the vertical proton beam positions predicted by using the ML.

TABLE III. Beam instrumentation and beam parameters monitored by the instrumentation. An open circle marks the parameter that can be detected using ML, while a triangle marks the parameter that will be tested in the future.

Beam parameter	BPM	PM	Beam CT	Horn CT	MM
Beam position	○	○			○
Beam spot size		○			△
Beam intensity			○		○
Horn current				○	○

VI. CONCLUSION AND FUTURE PROSPECTS

The NuMI horn focusing mechanism has been investigated by analyzing the observed muon monitor signals in the beam scan. The results suggest that the horn focusing magnet is a linear optics element, which has been confirmed by both analytical models and numerical simulations. Moreover, we have employed machine learning to deconvolve the horn current and beam intensity from the observed muon profile. The trained ANN model has demonstrated high accuracy in detecting the horn current and the beam intensity within $\pm 0.05\%$ and $\pm 0.1\%$ accuracy, respectively. Additionally, the ML approach has enabled us to detect the beam position at the target with an accuracy of ± 0.018 mm and ± 0.013 mm for the horizontal and vertical positions, respectively, from the observed muon profile. As expected, the detection accuracy is consistent with the accuracy of the primary beam instrumentation. Our current focus is on enhancing the ML's performance by preparing a training dataset with low systematic uncertainty and developing an algorithm to detect anomalous events.

The results of this study suggest that the muon monitor can be used as the secondary beam instrumentation

to monitor the beam parameters related to the NOvA physics tolerance with high accuracy. Muon monitors provide a significant benefit when validating measurements. Additionally, the study results indicate that Fermilab's Long Baseline Neutrino Facility (LBNF) might benefit from this technique.

Other secondary detectors, such as beam detectors located near the target, are highly effective in directly detecting secondary particles escaping from the target. However, it is worth noting that these detectors may not be reliable under extreme radiation conditions. Hence, upgrading the muon monitors should be considered to extend their functionality and reliability. Because the horn is a linear optics element, the muon profile on the muon monitor results from the chromaticity of the horn magnets. The chromaticity measurement can be obtained by observing the time-of-flight (TOF) of muons at various muon monitor channel locations. The correlation can be replicated in the full model simulation, and the initial pion energy spectrum will be reconstructed from the observed time domain muon profile. Ultimately, these are a resource to reconstruct the initial pion phase space.

It is found that the full-model simulation closely replicates the beam scan result. However, the observed muon profile is not accurately reproduced by the simulation.

The fine tuning is required in simulation. Two background signals on the muon monitors, namely the delta rays from high energy muons and excess particles created by the elastically scattered protons interacting in the absorber, must be evaluated to ensure accurate simulation. The hadronic interaction model needs to be tuned to replicate the measurements. Those studies are currently underway and will be published in separate papers.

ACKNOWLEDGMENTS

We would like to thank the Fermilab Accelerator Operations, Target Systems, External Beam Delivery, and Main Injector Departments for their contributions to this study. We also want to thank the NOvA collaboration for providing us with an opportunity to run the special beam tests.

This work is supported by the Fermi Research Alliance, LLC manages and operates the Fermi National Accelerator Laboratory pursuant to Contract number DE-AC02-07CH11359 with the United States Department of Energy.

This work is partially supported by the U.S. Department of Energy grant DE-SC0019264.

-
- [1] M. A. Acero *et al.* (NOvA), First Measurement of Neutrino Oscillation Parameters using Neutrinos and Antineutrinos by NOvA, *Phys. Rev. Lett.* **123**, 151803 (2019), arXiv:1906.04907 [hep-ex].
 - [2] P. Adamson *et al.* (NOvA), First measurement of electron neutrino appearance in NOvA, *Phys. Rev. Lett.* **116**, 151806 (2016), arXiv:1601.05022 [hep-ex].
 - [3] P. Abratenko *et al.* (MicroBooNE), Measurement of the flux-averaged inclusive charged-current electron neutrino and antineutrino cross section on argon using the NuMI beam and the MicroBooNE detector, *Phys. Rev. D* **104**, 052002 (2021), arXiv:2101.04228 [hep-ex].
 - [4] R. Acciarri *et al.* (MicroBooNE), Design and Construction of the MicroBooNE Detector, *JINST* **12** (02), P02017, arXiv:1612.05824 [physics.ins-det].
 - [5] ICARUS Collaboration, Icarus at the fermilab short-baseline neutrino program – initial operation (2023).
 - [6] C. Farnese *et al.* (ICARUS), Implementation of the trigger system of the ICARUS-T600 detector at Fermilab, *Nucl. Instrum. Meth. A* **1045**, 167498 (2023).
 - [7] L. Cremonesi, NOvA-DOCDB NOVA Document 17608-v5 (2017) internal technical note.
 - [8] P. Adamson *et al.*, The NuMI Neutrino Beam, *Nucl. Instrum. Meth. A* **806**, 279 (2016), arXiv:1507.06690 [physics.acc-ph].
 - [9] R. Acciarri *et al.*, *Long-Baseline Neutrino Facility (LBNF) and Deep Underground Neutrino Experiment (DUNE): Conceptual Design Report, Volume 1: The LBNF and DUNE Projects*, Tech. Rep. (DUNE, 2016) arXiv:1601.05471 [physics.ins-det].
 - [10] R. Acciarri *et al.*, *Long-Baseline Neutrino Facility (LBNF) and Deep Underground Neutrino Experiment (DUNE): Conceptual Design Report, Volume 2: The Physics Program for DUNE at LBNF*, Tech. Rep. (DUNE, 2015) arXiv:1512.06148 [physics.ins-det].
 - [11] J. Hylen, MINOS-DOCDB MINOS Document 6122-v1 (2009) internal technical note.
 - [12] R. Zwaska *et al.*, Beam-Based Alignment of the NuMI Target Station Components at FNAL, *Nucl. Instrum. Meth. A* **568**, 548 (2006), arXiv:physics/0609106.
 - [13] J. Crisp, B. Fellenz, J. Fitzgerald, D. Heikkinen, and M. A. Ibrahim, Operation of the intensity monitors in beam transport lines at fermilab during run II, *Journal of Instrumentation* **6** (10), T10001.
 - [14] J. Hylen and K. Yonehara, Beams-DOCDB Beams Document 9520-v1 (2018) internal technical note.
 - [15] L. J. Loiacono, *Measurement of the Muon Neutrino Inclusive Charged Current Cross Section on Iron Using the MINOS Detector*, Ph.D. thesis, University of Texas Austin (2010).
 - [16] R. M. Zwaska, *Accelerator Systems and Instrumentation for the NuMI Neutrino Beam*, Ph.D. thesis, University of Texas Austin (2005).
 - [17] <https://www.muonsinc.com/Website1/G4beamline>.
 - [18] E. Regenstreif, Technical Report 64-41 (CERN, 1961) internal technical note.
 - [19] H. Wiedemann, *Particle Accelerator Physics* (Springer Press, 2015).